buildings

MDPI

Article

Aspects of Modeling Prestressed Concrete Sleepers Subjected to Positive Moment Test at Midspan

Ricardo P. Randi [1], Leandro M. Trautwein [1,*] and Antônio C. dos Santos [2]

[1] Departamento de Estruturas, Universidade Estadual de Campinas, Campinas 13083-970, Brazil; r180462@g.unicamp.br
[2] Faculdade de Engenharia Civil, Federal University of Uberlândia, Uberlândia 38408-100, Brazil; acds@ufu.br
* Correspondence: leandromt@unicamp.br

Abstract: This paper aims to discuss aspects of modeling prestressed concrete sleepers based on experimental results. Midspan Positive Moment tests were performed on four prestressed sleepers. Using the ATENA 3D software, based on the Finite Element Method, numerical models were simulated through nonlinear analysis to adequately represent the behavior of the sleepers. To evaluate the influence of the crack model, the Young's modulus, and the fracture energy, a parametric numerical analysis was performed, varying these parameters in stages to achieve a more realistic model. The crack model was evaluated by modifying the "fixed crack model" to a "rotated crack model" while the Young's modulus and fracture energy were penalized by 0.00%, 5.00%, 10.00%, and 15.00% in relation to the value calculated according to the CEB FIP Model Code (2010). The numerical model with the "rotated crack model" and penalties of 0.00% and 5.00% for the Young's modulus and fracture energy, respectively, presented a better approximation to the results presented in the experimental tests. Finally, from this calibrated model, an experimental versus numerical comparative analysis was performed, comparing the load versus displacement curves, failure loads, maximum displacements, and crack pattern behavior. In the future, constitutive models of bond slip and expansive reactions will be applied to the calibrated model.

Keywords: prestressed concrete sleepers; experimental tests; numerical analysis; parametric analysis; constitutive models

check for updates

Citation: Randi, R.P.; Trautwein, L.M.; dos Santos, A.C. Aspects of Modeling Prestressed Concrete Sleepers Subjected to Positive Moment Test at Midspan. *Buildings* **2024**, *14*, 2387. https://doi.org/10.3390/buildings14082387

Academic Editor: Mizan Ahmed

Received: 8 June 2024
Revised: 23 June 2024
Accepted: 24 July 2024
Published: 2 August 2024

Copyright: © 2024 by the authors. Licensee MDPI, Basel, Switzerland. This article is an open access article distributed under the terms and conditions of the Creative Commons Attribution (CC BY) license (https://creativecommons.org/licenses/by/4.0/).

1. Introduction

Sleepers are one of the fundamental elements in the superstructure of railway tracks. In summary, their main functions including supporting the rails, keeping the track axis constant, and transmitting to the ballast vehicle axle loads, such as horizontal (transverse and longitudinal) and vertical actions. These functions make it necessary to provide the sleeper with a high resistance, which generally makes for great rigidity. At the same time, the sleeper must have a certain level of elasticity, enabling it to withstand high-impact forces [1].

The first sleepers used in railroads were wooden, with concrete sleepers introduced in the mid-twentieth century and consisting of a block of reinforced concrete with a constant section. These reinforced concrete sleepers underperformed due to the excessive vibration and impact to which they were subjected, leading to the appearance of cracks. Over time, it was noted that the main problem with cracking in reinforced concrete sleepers was reinforcement corrosion, due to reinforcement exposure. Sleepers in prestressed concrete began to be used, mainly after the 1940s, with the aim of controlling cracking [2].

It is important to point out that research on concrete sleepers is quite diversified, addressing topics related to sleeper behavior in static and dynamic tests, structural performance, and service performance. Additionally, existing studies also explore pathologies affecting durability, application of new materials in manufacturing, and numerical simulation.

According to [3], the failure modes of concrete sleepers in service are more varied when compared to the failure modes that occur in experimental tests. The authors note that the pattern and severity of cracks are important factors in the evaluation of sleepers, and that static bending tests at the rail seat and at the middle of the span are used to identify the formation and propagation mechanisms of these cracks in concrete sleepers. The midspan and support sections of the rail are more susceptible to cracks, according to [4].

The aforementioned tests are based on normative prescriptions for approval of sleepers in terms of bending moment effects. Normative codes, such as [5–7], comprise the general provisions for conducting these tests and designing sleepers. Ref. [8] conducted a comparison of material requirements and the production standards for concrete sleepers across American, European, and Chinese contexts.

Ref. [9] conducted static and dynamic tests on aged sleepers, including Positive Moment tests at the midspan [9]. The authors state that the initial cracking appeared under the load application point and at the middle of the span. Later, they observed the concrete crushing below the load application point, with the sleeper exhibiting softening behavior, resulting in decreased resistance and a gradual increase in displacement. Similar findings were reported in the work of [10].

Refs. [11,12] investigated the failure behavior of prestressed concrete sleepers, considering principles of non-linear fracture mechanics. The authors conducted bending tests with an opening at the middle of the span to analyze crack evolution and the resulting decrease in sleeper resistance. The authors observed that the first cracks appear in the center, followed by lateral cracks influenced by shear. They concluded that the influence of shear damage leads to the rupture of the sleeper. Ref. [13] addressed the damage to concrete sleepers from the perspective of the state of deformation and cracking in static or dynamic loads, including inspections of the rail seat of used sleepers.

Estimating the service time of a concrete sleeper is crucial for assessing the viability of railway maintenance costs. Time-dependent intrinsic factors of concrete can significantly influence the behavior of these elements. Between 2017 and 2020, a group of researchers published several works evaluating the impact of creep and retraction on the durability of sleepers; among these works, it is important to mention [14–17]. An important finding by the authors is that these phenomena may lead to loss of pretension of the wires over time.

One way to control excessive cracking in concrete sleepers, whether due to static and dynamic impacts or time-dependent phenomena, is the application of composite materials to concrete to improve its mechanical properties. Ref. [18] conducted static and impact tests on the support section of sleeper rails with and without the addition of synthetic macro fibers, concluding that the use of these fibers made the sleeper more ductile and reduced the opening of cracks. To produce hybrid sleepers, ref. [19] added fiberglass-reinforced polymer to concrete, reaching similar conclusions as [18]. This indicates that the proposal is a viable alternative for producing sleepers.

In a numerical context, refs. [2,20,21] simulated prestressed concrete sleepers applying fracture mechanics approaches. Ref. [17] analyzed the behavior of prestress loss in sleepers affected by creep and shrinkage of concrete through simulations. Using probabilistic models, ref. [22] analyzed the failure of prestressed sleepers affected by corrosion, and ref. [23] performed a comparative experimental versus numerical analysis of sleepers affected by ice expansion.

Although several studies have employed a numerical approach, few emphasize the influence of concrete's mechanical properties on the results of comparisons between experimental tests and numerical models. Generally, the calibration of numerical models is performed through comparative experimental versus numerical analyses, with the mechanical properties calculated from normative codes, such as in [24] and the implementation of pre-established constitutive models. In some cases, differences in the structural behavior of these simulations can lead to unsatisfactory results.

With the objective of calibrating a numerical model based on the Finite Element Method, this paper proposes a parametric numerical nonlinear analysis of the crack model

and two mechanical properties—the Young's modulus and fracture energy. It is noteworthy that obtaining numerical models that adequately simulate in-service behavior is a critical tool, mitigating costs associated with experimental tests and enabling the monitoring of different points of the structural elements. Subsequently, constitutive models of bond slip between steel–concrete and expansive reactions will be implemented to mitigate the loss of adherence between materials during these expansive processes.

Furthermore, the experimental results will be useful as a benchmark for future studies on concrete sleepers.

2. Experimental Tests

2.1. Sleepers in Prestressed Concrete

In total, four monoblock sleepers were experimentally tested at the Laboratory of Structures and Materials of the Federal University of Uberlândia on 25–27 October 2022. The four prestressed concrete sleepers had the same geometry, each with 16 prestressing wires measuring 6.00 mm in diameter, subjected to an initial prestressing force of 32.11 kN, equivalent to an initial deformation of 0.588%. The average compressive strength of concrete was 88.85 MPa. The steel was of the low relaxation type, notched, and with a resistance class of 1560/1750 MPa, according to [25–27]. Figure 1 shows the geometry of the sleepers.

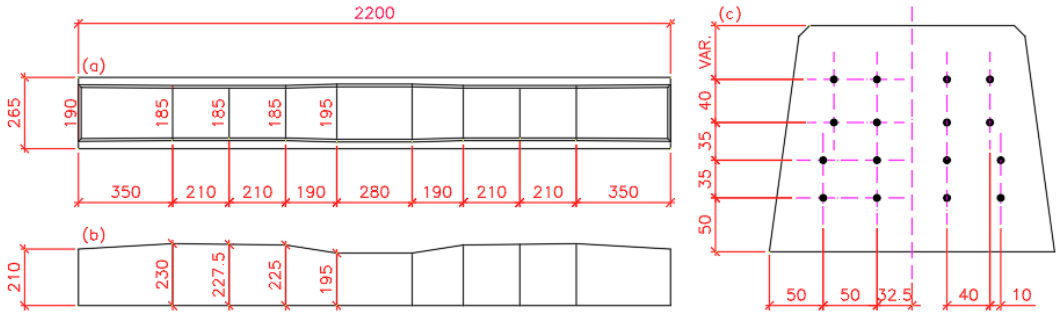

Figure 1. Sleeper geometry: (**a**) plan view, (**b**) lateral view e, (**c**) distribution of prestressing wires in cross section. Measurements in millimeters. Source: Author.

The four prestressed concrete sleepers were subjected to the Positive Moment test at the midspan, based on [5,6] standards, highlighting that the setups of the tests presented in both standards are similar. The aforementioned standards indicate the performance of several bending tests, including Positive Moment at the midspan, Positive Moment at the rail support, Negative Moment at the midspan, and Negative Moment at the rail support, to homologate the manufactured sleepers. It is noteworthy that the normative tests are conducted with the aim of verifying, mainly, the bending moments related to the opening of the first visible cracks.

In the experimental tests conducted in this research, the sleepers were subjected to loads until the specimens ruptured, since the objective of the tests was not to homologate the sleepers, but to use the results to calibrate the numerical model.

The Midspan Positive Moment test involved applying a load to the center of the sleeper, which rested on two supports made up of a set of metal sheets and rubber. Figure 2 shows the test setup.

Where:

A: Shore A 50 hardness rubber strip measuring 2″ × 1″ × 300.00 mm (length × thickness × width);

B: Shore A 50 hardness rubber strip measuring 1″ × 1/2″ × 300.00 mm (length × thickness × width);

C: Steel plate with dimensions 200.00 mm × 3/4″ × 600.00 mm (length × thickness × width);

D1: Steel plate with dimensions 125.00 mm × 1/2" × 230.00 mm (length × thickness × width);

D2: Steel plate with dimensions 150.00 mm × 1" × 150.00 mm (length × thickness × width);

E: 500.00 kN load cell;

F: Manual hydraulic actuator, supported by a metallic gantry of 800.00 kN;

G: Rigid metal apparatus to support the plates, resting on the reaction slab.

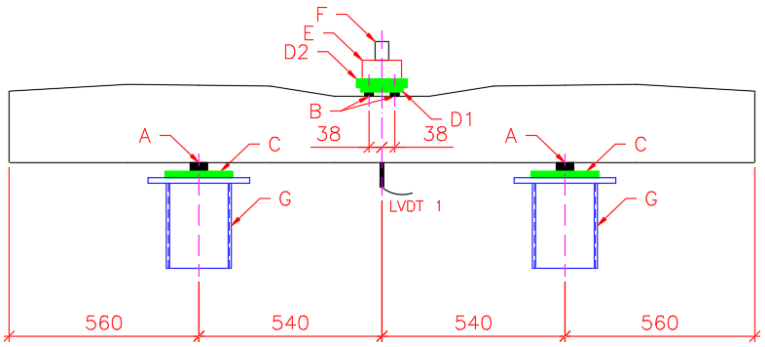

Figure 2. Setup of the Positive Moment test in the Midspan, measurements in millimeters. Source: Author.

An LVDT (100.00 mm range) was placed in the center of the sleepers to measure the displacements throughout the tests. The manual hydraulic actuator applied a load speed of 25.00 kN every 30.00 s, and the cracks were marked with a marker pen at each load application stop. Notably, the test continued until the sleepers ruptured. Figure 3 shows the setup of the assembled test.



Figure 3. Test setup of a sleeper carried out in the laboratory of the Federal University of Uberlândia. Source: Author.

2.2. Rubbers

During the experiments, it was noted that at the beginning of the tests, there is a great accommodation of the rubbers arranged below the load application plate and, mainly, of the supports. This fact was also verified during numerical modeling, where simulating this accommodation at the beginning of the test posed some difficulties, which will be discussed later.

To obtain a deformation magnitude of the rubbers under the application of compressive loads, tests were performed on four rubber strips: two new strips with the dimensions presented above and two previously used strips from the sleeper tests, also with the dimensions shown above (items A and B, below Figure 2).

The purpose of testing new and used rubber strips was to analyze whether the rubber loses rigidity after being reused in four tests of sleepers. Tests of strips with different

dimensions were conducted to assess the influence of form factor in elastomeric materials, according to [28,29]. Figure 4 shows a test on one of the rubber strips. The tests were performed using plates with dimensions close to those of the contact surfaces between the rubber and the sleeper, and the maximum compression load was approximately half of the breaking load of the sleepers, as each rubber receives this portion of load during the sleeper rupture test.



Figure 4. Setup for testing rubber strips. Source: Author.

2.3. Results of Experimental Tests

This study presents results related to the load versus displacement curves, the crack opening loads, and the final crack pattern of the four experimentally tested prestressed concrete sleepers. The nomenclature used for the specimens will be PCS (Prestressed Concrete Sleeper) followed by numbers 1, 2, 3, and 4, respectively, for PCS1, PCS2, PCS3 and PCS4.

The compressive strength of the sleeper concrete was obtained through tests on cylindrical specimens, according to [30]. The average of these results was considered 88.85 MPa on the date of the sleeper tests and 45.30 MPa on the date of application of the prestressing. The prestressing wires underwent tension, according to [31], yielding average results of 1709.90 MPa for tension at 1.00% strain, 1781.90 MPa for tensile strength, and Young's modulus of 193,151.0 MPa. It is noteworthy that these values were used in the numerical simulation.

2.3.1. Load–Displacement Curves from Experimental Tests

During the execution of the tests, a great accommodation of the rubbers used in the supports and in the point of application of the loads was noticed. It was observed that initially, the sleepers do not bend, the displacement primarily being a consequence of the accommodation of the supports' rubbers. Figure 5 presents the load–displacement curves of (a) the four sleepers and (b) the tests performed on the rubbers in order to verify their behavior. Displacements in the sleepers were measured through an LVDT positioned in the center of each specimen (see Figure 2), while the displacements of the rubbers were measured directly from the machine in which the test was performed. The nomenclature used in (b) is as follows: SRN, Support Rubber New; SRU, Support Rubber Used; LRN, Load Rubber New; and LRU, Load Rubber Used.

Analyzing the graph in Figure 5a, it is evident that all four specimens exhibited similar behavior in their load versus displacement curves. Notably, the LVDT of the PCS1 sleeper stopped measuring the displacements for a load of approximately 200.00 kN. A change in the stiffness of the sleepers is also observed for a load of approximately 50.00 kN. This first stage of the test was characterized by the accommodation of the support devices, presenting initial displacements in the test between 4.00 mm and 5.50 mm. Between loads of 50.00 kN and 150.00 kN, the ties showed linear elastic behavior.

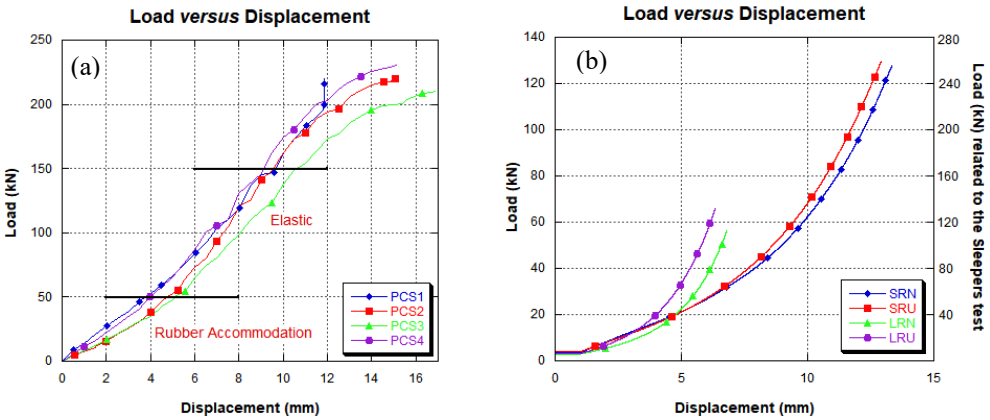

Figure 5. Load versus displacement curves (**a**) of sleepers and (**b**) of rubbers. Source: Author.

These observations are important, as the results in Figure 5b show that for a load of approximately 25.00 kN (50.00 kN relative to the sleeper test), the rubbers used in the supports show an exponential increase in stiffness, with displacements above 5.00 mm. Still analyzing Figure 5b, it is noted that the stiffness of rubbers varies with different geometries, explained by the form factor and characteristic of elastomer materials. Regarding the reuse of rubbers in the tests, there were few differences in the results, mainly in the rubbers of the supports. To discard the support accommodation region, obtain the sleeper linear behavior, and help the numerical analysis performed later, the first 50.00 kN of the tests conducted on the sleepers were discarded. A linearization of the straight lines that characterize the linear elastic behavior from the sleepers to the origin of the graph was performed. Figure 6 shows the load versus displacement curves of the sleepers after the changes made to the curves.

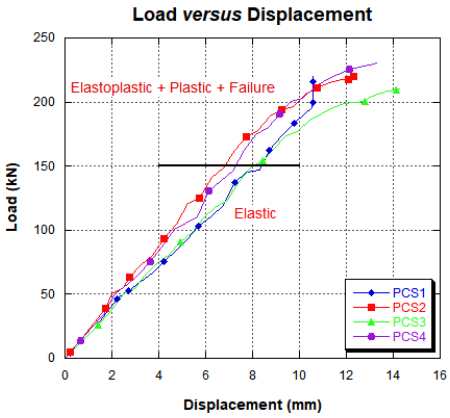

Figure 6. Load versus sleeper displacement curves after linearization of the curves. Source: Author.

The load–displacement curves of the four sleepers exhibited two different behaviors throughout the tests. Initially, up to approximately 150.00 kN, there was an elastic behavior, in which the sleepers showed linear displacements of low magnitude due to the rigidity of the specimens. After 150.00 kN, the elastoplastic and plastic phases began, followed by the rupture of the sleepers, with the elastoplastic and plastic phases proving difficult to perceive by the curves. Notably, in this second stage, the displacements increased sharply, due to the specimens' loss of rigidity, as a result of the appearance of cracks on the sleepers.

Finally, Table 1 presents the results of the rupture loads ($F_{_rup}$) and the maximum displacements of the models—namely, the maximum displacement of the original curves ($\delta_{_o}$) and maximum displacement of the linearized curves (δ). The offsets between the original and linearized curves are also presented to evaluate the discounted displacements in each specimen.

Table 1. Results of rupture loads and displacements of sleepers.

Sleeper	F_{rup}	δ_o	δ	Offset
	(kN)	(mm)	(mm)	(mm)
PCS1	220.00	11.85	10.56	1.29
PCS2	220.00	15.15	12.39	2.76
PCS3	210.00	16.86	14.28	2.58
PCS4	230.00	15.12	13.28	1.84
Average	220.00	14.75	12.63	2.12

2.3.2. Final Crack Pattern, Crack Opening Load, and Failure Mode

The cracks visible throughout the test were marked with a marker pen at each stop of load application (25.00 kN every 30 s) until the specimens ruptured. It should be noted that the cracks were marked, in most cases, only at the stopping point of the load application, and there may have been cases in which the cracks evolved between load steps. Figure 7 shows the final views of cracking of sleepers (a) PCS1, (b) PCS2, (c) PCS3 and (d) PCS4.

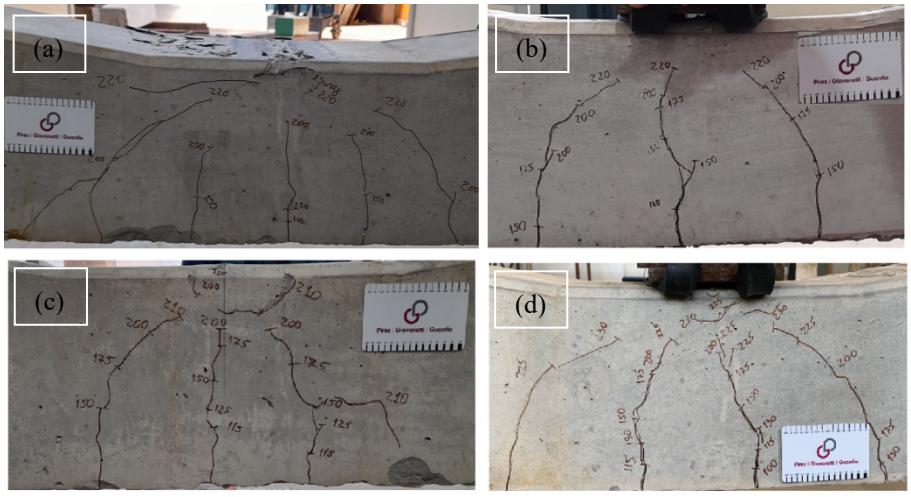

Figure 7. Final crack pattern views: (**a**) PCS1, (**b**) PCS2, (**c**) PCS3 and (**d**) PCS4. Source: Author.

The images of the final crack patterns presented in Figure 7 show that there is not exactly the same behavior in relation to the cracking of the sleepers, with the number of main cracks that evolve above the middle of the sleeper varying between 3, 4 and 5. In general, centralized cracks tend to evolve in a straight line, without inclinations, while decentralized cracks tend to incline from the region of the second reinforcement layer, being influenced by the shear effect—a phenomenon also observed by [11]. Considering that during this test, the sleeper behaves like a prestressed beam without shear reinforcement, this cracking scenario is consistent with the behavior of elements without transverse reinforcement.

It is noteworthy that the crack openings at the end of the test reached a maximum magnitude between 0.80 mm and 1.20 mm in the lower and central regions of the sleepers, with an average of 1.00 mm. The cracks observed in the upper regions of the sleepers (above the middle of the sleeper, i.e., the lateral face) were of small magnitudes, from approximately 0.05 mm to 0.10 mm.

Regarding the failure mode, the four sleepers exhibited similar behavior, with the crushing of the concrete in the upper central region of the section and also on the upper face of the sleepers, influenced by the point and mode of load application. As shown in Figure 8, these results corroborate the observations by [9]. In the upper region of the sleeper (upper face), cracks of small magnitudes were observed, between 0.05 mm and 0.10 mm.



(**a**) (**b**)

Figure 8. Rupture of the upper face of the sleeper: (**a**) PCS1 and (**b**) PCS3. Source: Author.

Table 2 presents the values of the rupture loads (F_{rup}), the maximum displacements (δ), the first centralized cracks (F_c), the first off-centered cracks (F_d), and the first inclined decentralized cracks ($F_{d,i}$). Percentage values are relative to rupture loads.

Table 2. Load of openings of the first visible cracks. Source: Author.

Sleeper	F_{rup}	δ	F_c		F_d		$F_{d,i}$	
	(kN)	(mm)	(kN)	(%)	(kN)	(%)	(kN)	(%)
PCS1	220.00	10.56 *	100.00	45.5	150.00	68.2	200.00	90.9
PCS2	220.00	12.39	115.00	52.4	150.00	68.2	175.00	79.6
PCS3	210.00	14.28	115.00	54.8	125.00	59.5	175.00	83.3
PCS4	230.00	13.28	100.00	43.5	150.00	65.2	200.00	87.0
Average	220.00	13.32	107.50	49.0	143.75	65.3	187.50	85.2

* value not considered in the average due to failure of the LVDT during the test.

The results presented in Table 2 reveal similar behavior for the four sleepers experimentally tested. It is observed that the cracks tend to appear centralized in loads that vary between 43.5% and 54.8%, with an average of 49.0%, that is, close to half of the rupture load. In all specimens, the decentralized loads appeared later than the centralized ones, and the inclined cracks appeared in the final stages of the test for an average value of 85.2% of the rupture load.

3. Numerical Simulations

A three-dimensional numerical simulation of prestressed concrete sleepers was performed, considering the non-linearity of the materials with the aid of the software tools GiD 15.0.3 and ATENA3D 5.9.0, based on the Finite Element Method. GiD 15.0.3 is a tool that assists in the pre-processing stage of models, allowing the modeling of geometry, mechanical properties of materials, boundary conditions, and finite element mesh. ATENA3D is a tool used for the processing and post-processing of models.

3.1. Constitutive Models

In this subsection, the constitutive models used in the simulations will be presented. A detailed description of these constitutive models can be found in [32], while the detailed description of the interface between GiD 15.0.3 and ATENA3D 5.9.0 can be found in [33].

Concrete was simulated using the constitutive model CC3DNonLinearCementitious2. According to [34], this model—the Fracture-Plastic Constitutive Model—is a combination of plasticization behavior in compression and fracture in tension. The non-linearity in compression is based on the failure surface of [35], considering the softening and hardening phenomena of the material. In tension, the nonlinear fracture behavior is based on [36] for the embedded crack in conjunction with the "crack band" model of [37]. A failure

criterion implemented by [38] was used for tensile failure, together with [39] an exponential softening function due to cracking.

According to [32], the uniaxial diagram of stress versus strain is divided in four states, with the diagram of concrete under tensile (states 1 and 2) and compressive (states 3 and 4) stresses. State 1 of the material is the pre-cracking tension, considered the linear elastic behavior, while state 2 is the post-cracking tension, characterized by the exponential crack opening law, based on [39]. State 3 is the behavior of the concrete before the stress peak—the same behavior presented in [24], and state 4 is the behavior of the concrete under post-peak compression, analogous to the Fictitious Crack Theory.

For the prestressed steel wires, the Reinforcement EC2 discrete model was implemented, presenting Uniaxial State of Stress based on Hooke's Law for the linear elastic region, as well as a plastification model based on the Von Mises Failure Criteria. The software GiD 15.0.3 enabled the parameterization of the prestressing wires, providing the characteristic curve of this type of reinforcement. It should be noted that possible slipping between wires and concrete was not simulated, thus using a perfect bond between the materials. The supports were simulated with a set of steel plates and Shore A 50 rubber, as described in Section 2.1. Steel plates were simulated using the constitutive model CC3DBiLinearSteelVonMises, with Von Mises Rupture Criteria and stress versus linear strain relationship in the elastic phase of the material. Shore A 50 type rubbers were simulated using the constitutive model CC3DElastIsotropic, with the stress versus strain relationship being linear for tension and compression.

The ATENA 3D software presents two cracking models, namely the "Fixed Crack Model", based on [40,41], and the "Rotated Crack Model", based on [42,43]. The "Rotated Crack Model" allows the crack to change direction while propagating, while the "Fixed Crack Model" stores the opening angle of the first crack and makes the propagation maintain this angle, changing direction only when a crack variation of 90° is registered in relation to the angle recorded at the beginning of the process [44]. A parametric numerical analysis of the crack models was performed and will be presented in Section 4.

3.2. General Description of Numerical Models

The geometry of the sleepers, prestressing wires, plates, and Shore A type rubbers were the same as those described in Section 2.1. Figure 9 presents the numerical model.

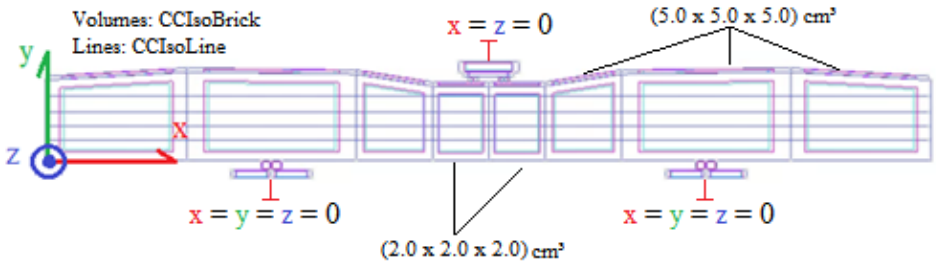

Figure 9. Numerical model, side view. Source: Author.

Two different loading intervals were implemented in the model—the first to apply prestressing to the steel wires and the second to apply the load.

The first interval was simulated with two load steps for prestressing application. The boundary conditions of this interval were imposed with the aim of simulating the sleeper at the time of concreting, with the imposition of restrictions in the x, y, and z directions on the lower face of the sleeper, simulating the support of the concreting position.

The second interval was simulated with 250 load steps for applying the load, with each load step representing 1.00 kN applied to the upper face of plate D2 (see Figure 2). The boundary conditions of this interval were imposed to simulate the sleeper during the Positive Moment test at the midspan, with the imposition of restrictions in the x and z directions on the upper face of the D2 steel plate and in the x, y, and z directions on the face bottom of the steel plates C (see Figure 2).

All connections between different finite elements were considered fixed (rigid connection between nodes), without the use of interface elements. Hexahedral elements were used for volume elements (concrete, plates, and rubber) and linear elements with two nodes were used for prestressing wires. Semi-structured meshes of approximately 2.00 cm were used in the central region of the sleeper, while semi-structured meshes of approximately 5.00 cm were used in the rest of the volume elements. The convergence criterion for resolving the problem was the Newton–Rhapson Method, with a maximum of 30 iterations and other default parameters of the computational program.

Finally, monitoring points were allocated to measure the reaction at the supports of the steel plates C. There were monitoring points to measure the displacements at the center of the upper faces of the four rubbers, and there was a monitoring point at the center of the sleeper to compare these displacements with the results of the LVDT allocated in the sleeper experimental tests (see Figure 2).

3.2.1. Mechanical Properties of Concrete

The compressive strength of concrete (f_c) implemented in interval 2 was 88.85 MPa—this value being obtained through testing on cylindrical specimens and Poisson coefficient 0.20. The mechanical properties described below were calculated based on [24], with the equations already implemented in the library of the software GiD 15.0.3. The characteristic tensile strength of concrete (f_{ct}) was calculated according to Equations (1) and (2), with average tensile strength (f_{ctm}) and characteristic strength to the minimum characteristic tensile strength ($f_{ctk,min}$), respectively. The initial Young's modulus was calculated according to Equation (3), and the fracture energy (G_f) was calculated according to Equation (4).

$$f_{ctm} = 2.12 \ln(1 + 0.1(f_{ck} + \Delta f) \quad (1)$$

$$f_{ctk,min} = 0.7 f_{ctm} \quad (2)$$

$$E_{ci} = E_{c0} \alpha_E \left(\frac{f_{ck} + \Delta f}{10} \right)^{\frac{1}{3}} \quad (3)$$

$$G_f = 73 {f_{ctk}}^{0.18} \quad (4)$$

For the characteristic tensile strength, the lower limit of resistance was used, and Δf equaled 8.00 MPa, resulting in f_{ct} = 3.52 MPa. For the Young's modulus, the values E_{c0} = 21,500.00 MPa, α_E = 1.00 (quartzolitic aggregates), and Δf = 8.00 MPa were used, resulting in E_{ci} = 45,828.80 MPa. Finally, the fracture energy (G_f) = 164.00 N/m. Notably, these values are the defaults of the computer program used.

The compressive strength of concrete (f_c) implemented in interval 1 (prestressing) of the numerical model was 45.30 MPa—this value being obtained through testing on cylindrical specimens and Poisson coefficient 0.20. The other mechanical properties of this concrete were also calculated based on [24], applying Equations (1)–(4).

3.2.2. Mechanical Properties of Prestressing Wires

The 16 prestressing wires were implemented with 1709.90 MPa for tension at 1.00% strain, 1781.90 MPa for tensile strength and Young's modulus of 193,151.80 MPa. The wires were simulated with the application of an initial strain of 0.588%, equivalent to an initial prestressing force of 32.11 kN, considering both ends of the wires to be free. It is important to point out that this was considered a perfect bond between steel and concrete, not simulating possible slipping of the wires, only those due to the opening of cracks, already considered by the software.

3.2.3. Mechanical Properties of Support Devices (Plates and Rubbers)

All steel plates were implemented with Young's modulus of 200.00 GPa, yield stress of 550.00 MPa, and Poisson coefficient 0.30.

Shore A 50 type rubbers were implemented as an elastic material with an elastic modulus that varied according to the level of compressive stress to which they were subjected. During the modeling, an attempt was made to approximate the displacements of the rubbers to the behavior of the load versus displacement curve shown in Figure 5b.

However, for very low values of Young's modulus (beginning of the curves shown in Figure 5b), the model proved to be unstable, with inadequate cracking in relation to that presented in the experimental tests. Conversely, for very high values of Young's modulus (end of the curves shown in Figure 5b), the model showed high stiffness, with very low maximum displacements.

Based on these observations, it was noted that the rigidity of the support devices exerts great influence on the sleepers' modeling. It was also observed that the rubbers of the support devices exert greater influence on the numerical results when compared to those of the loading point. To establish average values for the deformations of the rubbers, average values of Young's modulus calculated from the graphs shown in Figure 5b were adopted.

For the beginning of the test up to approximately 50.00 kN of load, the Young's modulus implemented was 15.00 MPa and 10.00 MPa for the support rubbers and load application rubbers, respectively. In a second stage, until the end of the test, the Young's modulus implemented was 20.00 MPa and 25.00 MPa for the support rubbers and load application rubbers, respectively.

4. Parametric Numerical Analysis

The parametric numerical analysis was performed to obtain a numerical model that represented behavior similar to that of the experimentally tested sleepers. Nine models were simulated by varying the crack model, Young's modulus, and fracture energy. The models were named with the prefix "PCSN" (Prestressed Concrete Sleeper—Numerical) followed by numbers 1 to 9.

4.1. Description of the Parametric Analysis Steps

The first step aimed to evaluate the crack model (PCSN1, PCSN2, PCSN3). The concrete crack model was varied from fixed crack model to rotated crack model, with coefficients of 0.75 and 0.50, respectively. According to [45], this coefficient determines the change from fixed crack model to rotated crack model. The coefficient 1.00 is a fixed direction from the beginning of the crack opening, while the coefficient 0.00 is a fully rotated crack. Values between 0.00 and 1.00 determine at what value of tensile stress in the concrete vis-à-vis the material's tensile strength the crack begins to rotate. Thus, the coefficient 0.50 represents an intermediate model between fixed and rotated cracks.

The second stage aimed to evaluate the Young's modulus of concrete (PCSN4, PCSN5, PCSN6). It was taken into account that the maximum displacement of the model is formed by the displacement of the rubbers added to the sleeper displacement due to bending. With the elasticity of the rubber defined earlier in 3.2.3, the sleepers were simulated by varying the Young's modulus of the concrete by 100.00%, 95.00%, 90.00%, and 85.00% in relation to the Young's modulus calculated by [24]. The results analyzed in this step are related to the maximum displacements and the breaking loads of the models when compared to the experiments.

The third and last step aimed to evaluate concrete's fracture energy (PCSN7, PCSN8, PCSN9), defined as the ability of concrete to resist cracking, or even the energy required for a single crack to propagate. From the model that presented the best result in relation to the Young's modulus of the concrete, new models were simulated, varying the fracture energy by 100.00%, 95.00%, 90.00%, and 85.00% in relation to the fracture energy calculated by [24]. The results related to the opening loads of the first crack, the models' crack pattern, the maximum openings of the cracks in addition to the maximum displacements, and the rupture loads will be analyzed.

Table 3 presents the mechanical properties of the nine numerically simulated models, namely compressive strength (f_c), tensile strength (f_{ct}), Young's modulus (E_c), and fracture energy (G_f).

Table 3. Mechanical properties of numerical models analyzed parametrically. Source: Author.

	f_c	f_{ct}	E_c		G_f		Crack Model	
	(MPa)	(MPa)	(%)	(MPa)	(%)	MN/m	Model	Coefficient
Sleeper	Parametric Analysis—Crack Model							
PCSN1	88.85	3.52	100.00	45,828.80	100.00	0.000164	Fixed	1.00
PCSN2							Rotated	0.75
PCSN3							Rotated	0.50
Sleeper	Parametric Analysis—Young's Modulus							
PCSN4	88.85	3.52	95.00	43,537.36	100.00	0.000164	Rotated	0.50
PCSN5			90.00	41,245.92				
PCSN6			85.00	38,954.48				
Sleeper	Parametric Analysis—Fracture Energy							
PCSN7	88.85	3.52	100.00	45,828.80	95.00	0.000156	Rotated	0.50
PCSN8					90.00	0.000148		
PCSN9					85.00	0.000139		

4.2. Parametric Numerical Analysis Results

To facilitate future analyses and discussions, Table 4 presents the results for the rupture loads (F_{rup}) and the maximum displacements (δ) of the experimentally tested sleepers of the nine numerical models, in addition to the numerical results. The values in percentages represent the differences between the rupture loads and the maximum displacements of the numerical models in relation to the average of the experimental tests.

Table 4. Results for rupture loads and maximum displacements of sleepers and numerical models. Source: Author.

Sleeper	F_{rup}		δ	
	(kN)	(%)	(mm)	(%)
Experimental tests				
PCS1	220.00	-	10.56 *	-
PCS2	220.00	-	12.39	-
PCS3	210.00	-	14.28	-
PCS4	230.00	-	13.28	-
Average	220.00	-	13.32	-
Numerical models				
PCSN1	195.00	11.4	10.11	24.1
PCSN2	185.00	15.9	9.22	30.8
PCSN3	220.00	0.0	12.70	4.6
PCSN4	203.00	7.7	12.08	9.3
PCSN5	210.00	4.6	12.15	8.8
PCSN6	213.00	3.2	12.30	7.6
PCSN7	220.00	0.0	13.17	1.1
PCSN8	216.00	1.8	12.38	7.0
PCSN9	208.00	5.5	11.12	16.5

* value not considered in the average due to failure of the LVDT during the test.

4.2.1. Parametric Numerical Analysis of the Crack Model

Analyzing Table 4, it can be observed that the PCSN3 model showed good proximity to the average of the experimentally tested sleepers. According to [46], the Rotated Crack Model tends to present lower rupture loads than the Fixed Crack Model. This finding is critical for analyzing the results of the PCSN1, PCSN2, and PCSN3 models, as the PCSN2 model corroborates the authors' findings, presenting a lower rupture load. The PCSN3 model, on the other hand, being a middle ground between the fixed and rotated models, presented a higher rupture load, which could lead to a wrong conclusion that the authors' finding does not fit in this case. However, when analyzing Figure 10, it is noted that the final crack patterns of the PCSN1 and PCSN2 models differ considerably in relation to the results of the experimental tests (see Figure 7), as they do not show inclined cracks. Conversely, the PCSN3 model presents behavior similar to that of the sleepers tested.

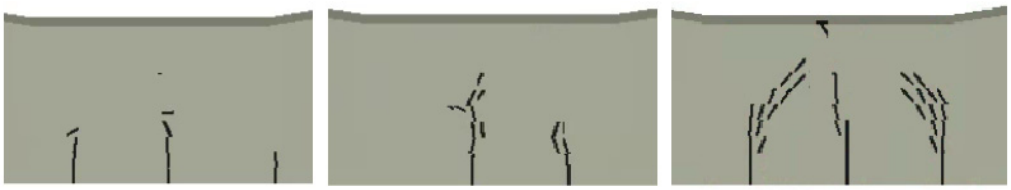

(**a**) (**b**) (**c**)

Figure 10. Final crack pattern views of models (**a**) PCSN1, (**b**) PCSN2 and (**c**) PCSN3 at failure load. Cracks limited to an opening of 0.05 mm. Source: Author.

Figure 10 presents the final crack patterns of models (a) PCSN1, (b) PCSN2, and (c) PCSN3 at rupture load.

Analyzing Table 4 and Figure 10, it can be seen that the PCSN3 model was closer to the behavior of the experimentally tested sleepers. The rupture load was equal to the average rupture load, and the maximum displacement showed a difference of 4.6% in relation to the average of the experimental tests. The crack pattern presents behavior similar to those shown in Figure 7. Based on these findings, the crack model adopted for the other six numerical models was the rotated crack model, with a coefficient of 0.50.

4.2.2. Parametric Numerical Analysis of the Young's Modulus

It is known that several factors affect the Young's modulus of concrete. Ref. [24] states that concrete's elastic deformations depend on the composition—mainly the type and size—of the aggregate, and can decrease and increase by up to 20.00% and 30.00%, respectively, depending on the aggregate type. In addition to the type of aggregate, factors such as creep and shrinkage can also influence the Young's modulus of concrete. According to [47], the formula indicated by [24] is more accurate when the parameters are adjusted by experimental creep tests. A discussion about the importance of evaluating, through experimental tests, the behavior of concrete over time to obtain more accurate results regarding the influence of phenomena such as creep and shrinkage on the properties of the concrete, including the Young's modulus, was pursued in [48].

It should be noted that the objective of this stage of the parametric analysis is not to discuss the intrinsic phenomena of concrete that affect the elasticity of the material. The authors and normative code mentioned above are cited to elucidate that there may be discrepancies between Young's modulus values when calculated by analytical equations without the support of experimental tests and greater knowledge of the material's composition.

The main objective of this stage is to obtain an adjusted value for the Young's modulus of the concrete implemented in the numerical simulations since, as previously discussed in Section 3.2.3, it was difficult to simulate the rubbers present in the support devices, and this material influences the stiffness of the model. With the properties of the rubbers defined, a parametric numerical analysis of the Young's modulus of the concrete comparing the

results of rupture load and deformations between numerical and experimental models can be an important tool for defining this mechanical property.

Analyzing the results presented in Table 4, it is concluded that the models with penalization of the Young's modulus presented lower rupture loads in relation to the PCSN3 model. As the rupture load values are different, to verify and compare the change in the stiffness of the numerical models, the displacements in the load step of 100.00 kN will be presented, that is, still in the models' linear behavior. The displacements for this load step were 4.59 mm, 4.62 mm, 4.64 mm, and 4.71 mm, respectively, for models PCS3, PCS4, PCS5, and PCS6. These results are consistent, as the greater the Young's modulus, the greater the stiffness and, consequently, the smaller the displacement.

Finally, it is noteworthy that the PCSN3 model, with the Young's modulus calculated by [24] and without penalizing this value, exhibited better behavior in relation to the parametric analysis of elasticity. Considering that the rigidity of the model is influenced, mainly, by the Young's modulus of the support device rubbers and the concrete and that the maximum displacement of the PCS3 model presented a difference of only 4.6% in relation to the average of the experimental tests, it can be concluded that the simulated model presents behavior similar to that of the experiments, even using an average Young's modulus for the rubbers.

4.2.3. Parametric Numerical Analysis of Fracture Energy

It is important to highlight that this step of the parametric analysis was performed only with alteration of the fracture energy values and that another valid approach would be to alter the tensile strength and, as a consequence, the fracture energy.

In the mid-1980s, RILEM published a recommendation for the calculation of fracture energy from a three-point test of beams. Several authors, including [49], carried out tests with the aim of validating the RILEM prescriptions. According to [50], several studies from that time concluded that the fracture energy is influenced by the size of the test specimen, the composition and age of the concrete, and curing methods. In a parametric numerical approach to slabs, ref. [51] concluded that the value of fracture energy in tension as well as the concrete softening model significantly influence the load versus displacement curve of the models.

Table 5 presents a summary of the results of the numerical models PCSN3, PCSN7, PCSN8 and PCSN9 in addition to the average of the experimental tests of the sleepers. In this stage, the results related to the opening loads of the first centralized crack (F_c), the models' crack pattern, the maximum crack openings (w_{max}), maximum displacements (δ), and the rupture loads (F_{rup}) were analyzed. The values in percentages represent the differences between the rupture loads and the maximum displacements of the numerical models in relation to the average of the experimental tests and also the opening load of the first crack in relation to the rupture load of each model.

Table 5. Summary of the results of the parametric fracture energy analysis. Source: Author.

Sleeper	F_{rup}		δ		F_c		w_{max}
	(kN)	(%)	(mm)	(%)	(kN)	(%)	(mm)
Experimental average							
Average	220.00	-	13.32	-	107.50	49.0	1.00
Numerical models							
PCSN3	220.00	0.0	12.70	4.65	119.00	54.1	1.10
PCSN7	220.00	0.0	13.17	1.13	119.00	54.1	1.00
PCSN8	216.00	1.8	12.38	7.06	118.00	54.6	0.95
PCSN9	208.00	5.5	11.12	16.52	118.00	56.7	0.85

The results in Table 5 show that the decrease in fracture energy influenced the rupture load and displacement of the models. In agreement with [50], models with higher values of fracture energy have a higher rupture load. Analyzing the results of the authors, it was possible to observe that for the same load, the models with lower fracture energy tend to present greater displacements, a fact also observed when comparing the maximum displacements of the PCSN3 and PCSN7 models, being respectively 12.70 mm and 13.17 mm for the same rupture load of 220.00 kN.

Regarding the openings of the first centralized cracks and the final crack pattern, there were few differences. Figure 11 shows the final crack dispersion of the four models, for a maximum crack width of 0.05 mm.

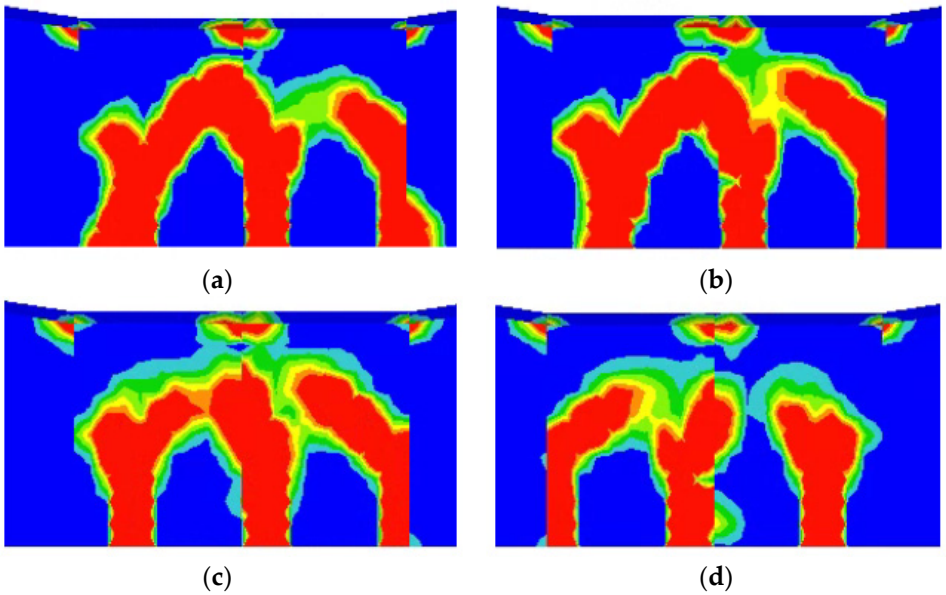

Figure 11. Final dispersion diagrams of the cracks of models (**a**) PCSN3, (**b**) PCSN7, (**c**) PCSN8 and (**d**) PCSN9. Source: Author.

Analyzing Figure 11, it is possible to verify that the four models presented behaviors similar to those presented in Figure 7 for the sleeper tests. An important observation is that the fracture energy significantly influenced the final crack pattern only for decreases from 85.00%. The PCSN9 model showed only one decentralized/inclined crack pointing to the crushing point of the concrete (central and upper), while the other crack had a smaller range in relation to the height of the sleeper.

Among the results presented in relation to the maximum opening of the cracks, the models presented a good response when compared to the maximum value of 1.00 mm observed during the experiments. Clearly, the PCSN8 and PCSN9 models have smaller openings, as the rupture loads are lower. It is important to point out that the PCSN3 and PCSN7 models showed a good approximation for the same average rupture load of the experimentally tested sleepers.

Finally, after a three-stage parametric analysis, it was concluded that the PCSN7 model was more similar to the sleepers tested. This numerical model was defined, in addition to the parameters presented in item 3.2, with a rotated crack model with coefficient 0.50, Young's modulus of 45,828.80 MPa and fracture energy of 0.000156 MN/m. The rupture load of the model showed equality in relation to the average rupture load of the tests (220.0 kN), the maximum displacement showed a difference of 1.1%, and the behavior in relation to cracking showed similarity when compared to the final crack patterns described in item 2.3.2.

5. Experimental Versus Numerical Comparative Analysis

With the objective of qualitatively evaluating the results of the numerical simulation, the results related to the load versus displacement curves, the crack opening loads and the final crack pattern of the numerical model, named PCSN (Prestressed Concrete Sleeper Numerical), will be presented, comparing these results to the results for experimentally tested sleepers, presented earlier in Section 2.3. The PCSN model is the PCSN7 model, being the model that presented the best performance in the parametric analysis.

5.1. Load Versus Displacement Curves

Figure 12 presents the load versus displacement curves, (a) before the offset and linearization of the curves and (b) after the offset and linearization of the curves of the experimental results.

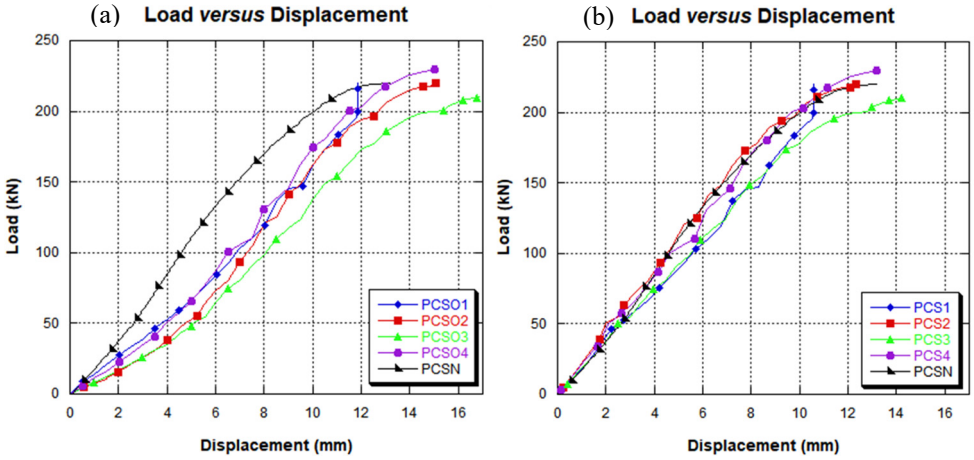

Figure 12. Load versus displacement curves of the experimental models and the numerical model. Source: Authors.

Analyzing Figure 12b, it is possible to verify the similarity between the numerical model and the experimental specimens. The numerically simulated model also presents a linear elastic phase up to a load of approximately 150.00 kN and, after this load, the behavior is elastoplastic until failure, as in the experiments carried out in the laboratory.

An important result to highlight is the final displacements of the rubbers positioned below the plate on which the load was applied and also in the supports of the numerical model, being 6.71 mm and 7.73 mm, respectively. In the experimental tests, these results were not obtained; however, these results demonstrate the importance of discarding the initial accommodation of the materials (rubber and concrete), a fact elucidated by the greater proximity of the load versus displacement curve in (b) when compared to (a). In fact, there were difficulties in adequately modeling the Shore A 50 rubber material due to the wide variation in the elastic modulus of the rubber when subjected to compression, and [5,6] standards indicate the use of these rubbers in the approval tests for sleepers. However, for tests used to calibrate numerical simulations, rigid supports made of wood or steel could be used instead of rubber, reducing the accommodation of the supports and making the offset between the curves less accentuated. Another option would be to measure the rubber displacements along the experimental tests; however, the positioning of LVDTs or extensometers in those regions is difficult due to the lack of space.

5.2. Final Crack Pattern, Crack Opening Load and Failure Mode

Table 6 shows the comparison between the results of the rupture loads (F_{rup}), the maximum displacements (δ), the first centralized cracks (F_c), the first decentralized cracks (F_d) and the first inclined decentralized cracks ($F_{d,i}$) for the experimentally tested sleepers and the PCSN numerical model. The openings of the first cracks in the numerical model were considered with an opening magnitude of 0.05 mm. The second part of Table 6

shows the results of the comparative analyses between the numerical model, each of the four sleepers, and the average of the experimental tests.

Table 6. General results of the experimental and numerical models and results of the comparative analysis. Source: Author.

Sleeper	F_{rup}	δ	F_c		F_d		$F_{d,i}$	
	(kN)	(mm)	(kN)	(%)	(kN)	(%)	(kN)	(%)
PCSN	220.00	13.17	119.00	54.1	133.00	60.5	176.00	80.0
PCS1	220.00	10.56 *	100.00	45.5	150.00	68.2	200.00	90.9
PCS2	220.00	12.39	115.00	52.3	150.00	68.2	175.00	79.6
PCS3	210.00	14.28	115.00	54.8	125.00	59.5	175.00	83.3
PCS4	230.00	13.28	100.00	43.5	150.00	65.2	200.00	87.0
Average	220.00	13.32	107.50	49.0	143.75	65.3	187.50	85.2
Comparative Analysis								
Relation	F_{rup}	δ	F_c		F_d		$F_{d,i}$	
	(%)	(%)	(%)		(%)		(%)	
PCSN/PCS1	0.0	-	19.0		11.3		12.0	
PCSN/PCS2	0.0	6.3	3.5		11.3		0.6	
PCSN/PCS3	4.8	7.8	3.5		6.4		0.6	
PCSN/PCS4	4.4	0.8	19.0		11.3		12.0	
PCSN/Average	0.0	1.1	10.7		7.5		6.1	

* value not considered in the average due to failure of the LVDT during the test.

Taking into account the results of the comparative analysis presented in Table 6, it appears that the numerically simulated model presents, in most cases, disparities smaller than 11.0% when compared to the average of the results of the experimentally tested specimens.

The relationships between rupture loads (F_{rup}) show proximities, with values below 5.0% of differences. The maximum displacement (δ) of the numerical model was closer to that of the PCS4 sleeper with a difference of 0.8%. Even with this greater proximity to the PCS4 sleeper, it can be seen in Figure 12b that the behavior of the load versus displacement curve between PCSN and PCS2 is closer, with little difference in stiffness.

Regarding the crack opening loads, it should be taken into account that the cracks were marked, in most cases, at each stop of load application in the experimental tests. Thus, the evolution of the cracks is conditioned not to be evaluated between load steps, which may generate greater deviations in the results. Even with that, the results are satisfactory mainly for the cases of the first centralized cracks (F_c) of the PCS2 and PCS3 sleepers, the first decentralized cracks (F_d) of the PCS3 sleeper and the first inclined decentralized cracks ($F_{d,i}$) of the PCS2 and PCS3 sleepers. In relation to the mean, the greatest disparities were for centralized cracks (F_c).

In general, the numerical model PCSN showed greater proximity to the PCS2 and PCS3 sleepers. Figure 13 presents the crack opening evolution of the numerical model in the load steps of (a) 119.00 kN, (b) 133.00 kN, (c) 176.00 kN and (d) 220.00 kN; the cracks are limited to 0.05 mm. The same figure shows the evolution of the normal stresses arising from the bending to which the sleeper is subjected throughout the test, and the range presented is limited superiorly by values greater than or equal to the tensile strength of the concrete of the simulated sleeper (3.52 MPa, in red).

Analyzing Figure 13, it can be seen that the cracks tend to evolve according to the evolution of the normal tensile stresses due to the bending imposed on the model. It should also be noted that three main cracks appeared, extending almost to the top of the sleeper,

with this behavior being the same as that of the PCS2 and PCS3 sleepers. This observation is important, because analyzing the results of Table 6, it is concluded that the numerical model PCSN showed greater proximity to the PCS2 and PCS3 sleepers.

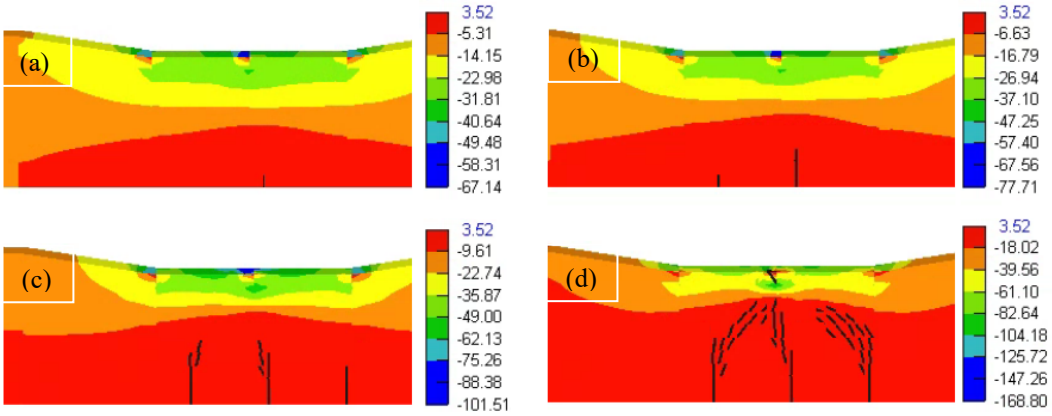

Figure 13. Evolution of cracks in the PCSN numerical model. Source: Author.

It is noted that, in line with what is shown in Figure 7 for the experimental specimens, the centralized crack tends not to incline, while the decentralized cracks incline from the height of the second line of prestressing wires, being influenced by shear, corroborating [12]. It is observed in (d) that the upper central region of the section reaches the tensile strength of the concrete and cracks, initiating the concrete weakening process, providing the concrete crushing failure mode, as evidenced by [9]. It is also observed that the three cracks evolve towards the region in which the crushing of the concrete will occur in the upper region.

Finally, an important finding is that cracks tend to evolve in a straight line (see Figure 13c) up to a load between 150.00 kN and 175.00 kN (experimental) and 176.00 kN (numerical), these values being approximately 80.0% of the rupture load, and after this load interval, they begin to tip. This crack inclination process coincides with the end of the linear elastic regime and the beginning of the elastoplastic regime of the sleepers.

Finally, Figure 14 presents (a) the final crack dispersion of the PCSN numerical model, (b) the final crack pattern of the PCS3 sleeper and (c) the overlapped images. The displayed range is limited superiorly by values greater than or equal to 0.05 mm, in red, and the cracks shown (in black) have a magnitude of 1.00 mm.

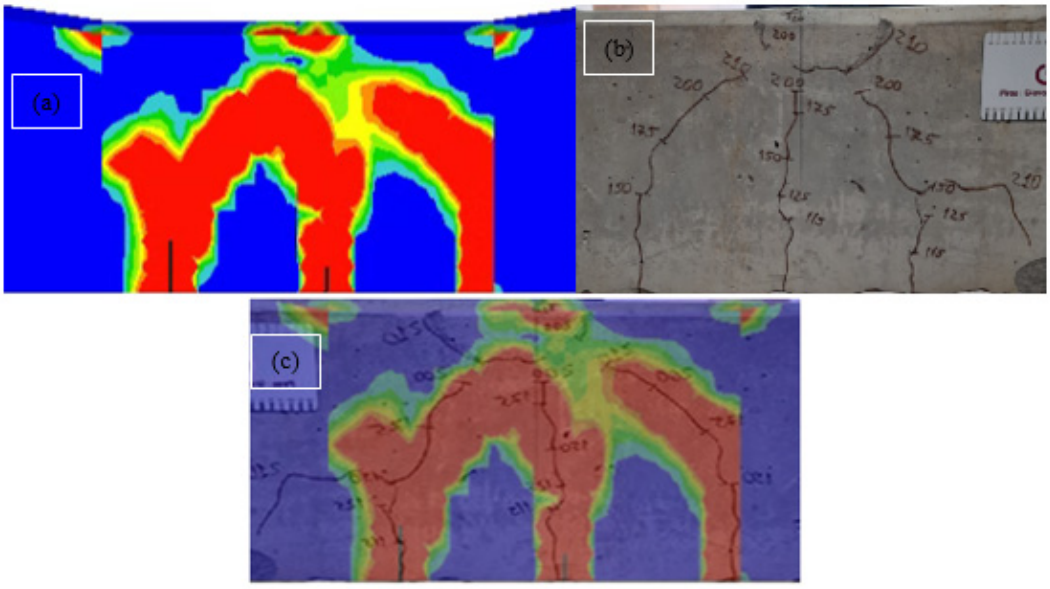

Figure 14. Final cracking views of (**a**) the numerical model PCSN, (**b**) experimental tested sleeper PCS3 and (**c**) overlapped images. Source: Author.

When comparing the final crack patterns shown in Figure 14, the similarity is noted. As the last comparative result presented in this subsection, it is noteworthy that the maximum magnitude of crack opening in the numerical model was 1.00 mm, while in the experimentally tested sleepers, the maximum magnitude of cracks was between 0.80 mm and 1.20 mm, in the lower regions of the sleepers. In the upper regions, above the second line of prestressing wires, the opening of the cracks ranged from 0.05 mm to 0.10 mm.

6. Conclusions

Nine models of prestressed concrete sleepers were numerically simulated through non-linear analysis and with the aid of the computational program ATENA 3D. These models were submitted to a parametric numerical analysis in order to calibrate the crack model parameters and the mechanical properties of Young's modulus and fracture energy. This calibration was performed by comparing the numerical results to the results of the experimental tests of four sleepers in prestressed concrete to evaluate which parameters lead to a model with a behavior closer to the real one.

The four sleeper specimens were submitted to the Positive Bending Moment test at the midspan, based on normative prescriptions. In general, the experimental results showed similarity between the specimens for load versus displacement curves, rupture loads, maximum displacements, crack patterns, and failure mode. It is noteworthy that the behavior of experimentally tested sleepers corroborated the work of [9].

During the experimental tests, it was verified that the use of rubbers in the supports leads to a great accommodation of the materials in the beginning of the test. Although the normative prescriptions indicate the performance of tests with these rubbers, the use of this material makes the numerical simulation difficult, as this material's elastic behavior presents great variation when subjected to compression. Therefore, the use of more rigid supports is indicated for calibration of numerical models.

The parametric numerical analysis was performed in three distinct steps. In the first stage, the crack model was varied into fixed crack model and rotated crack model, and the second model presented results closer to those observed in the experimental tests, highlighting that the first model proved to be unsatisfactory. The other two steps were related to the calibration of the following parameters: Young's modulus and fracture energy, calculated by [24] and penalized at 0.00%, 5.00%, 10.00% and 15.00%. Both results show that the penalized models present a lower rupture load in relation to the average of the specimens, as the model with a 100% Young's modulus was more satisfactory, presenting a divergence of 4.6% in relation to the average maximum displacement. As for fracture energy, the results corroborated with [50] and showed influence on the behavior of the models only for penalties of 15.00%. It is concluded that the crack model had the greatest influence on the parametric numerical analysis, followed by the fracture energy and, finally, the Young's modulus.

Finally, from the calibrated model, the results were compared to the experimental tests. The results were satisfactory, mainly when compared to specimens PCS2 and PCS3, showing greater similarity. It is noteworthy that the variations in rupture loads, maximum displacements and crack behavior showed differences of a maximum of 6.4% and structural behavior close to reality. The evolution of the cracks in the models was similar to that observed in the experiments, with rectilinear centralized cracks and inclined decentralized cracks, being influenced by the shear effect, corroborating the observations of [11].

As a consequence of the calibration of the model that adequately represents the behavior of the sleepers experimentally tested, constitutive models will be implemented with the aim of analyzing the influence of the loss of adherence between steel and concrete due to the action of expansive reactions in the concrete. For this, a bond slip constitutive model and an expansive reaction constitutive model will be implemented.

Author Contributions: R.P.R.: Conceptualization, Formal analysis, Investigation, Methodology, Validation, Writing—original draft, Writing—review and editing. A.C.d.S.: Supervision, Visualization, Writing—review and editing. L.M.T.: Supervision, Formal analysis, Methodology, Visualization, Writing—review and editing. All authors have read and agreed to the published version of the manuscript.

Funding: This research was funded by VALE S.A.

Data Availability Statement: Data available on request from the authors.

Acknowledgments: Thanks to the Federal University of Uberlândia (UFU) and the private company VALE S.A., who made this research viable by providing financial support and the necessary tools.

Conflicts of Interest: The authors declare no conflicts of interest.

Abbreviations

E_{ci}	initial Young's modulus
F_rup	rupture load
f_c	compressive strength of concrete
F_c	load of the first centralized cracks
f_{ck}	characteristic strength of concrete
f_{ct}	characteristic tensile strength of concrete
$f_{ctk,min}$	minimum characteristic tensile strength
f_{ctm}	average tensile strength
F_d	load of the first off-centered cracks
$F_{d,i}$	load of the first inclined decentralized crack
G_f	fracture energy
w_{max}	maximum crack opening
δ	maximum displacement of the linearized curves
δ_o	maximum displacement of the original curves

References

1. Bastos, P.S.S. Análise Experimental de Dormentes de Concreto Protendido Reforçados com Fibras de Aço. Ph.D Thesis, Engineering School of São Carlos, University of São Paulo, São Carlos, Brazil, 1999.
2. Silva, R.; Silva, W.V.; de Farias, J.Y.; Santos, M.A.A.; Neiva, L.O. Experimental and Numerical Analyses of the Failure of Prestressed Concrete Railway Sleepers. *Materials* **2020**, *13*, 1704. [CrossRef] [PubMed]
3. Taherinezhad, J.; Sofi, M.; Mendis, P.; Ngo, T. A review of behaviour of prestressed concrete sleepers. *Electron. J. Struct. Eng.* **2013**, *13*, 1–16. [CrossRef]
4. Domingo, L.M.; Martín, C.Z.; Avilés, C.P.; Herráiz, J.I.R. Analysis of the influence of cracked sleepers under static loading on ballasted railway tracks. *Sci. World J.* **2014**, *2014*, 1–10. [CrossRef] [PubMed]
5. Associação Brasileira de Normas Técnicas. *NBR11709—Dormente de Concreto—Projeto, Materiais e Componentes*; Associação Brasileira de Normas Técnicas: Rio de Janeiro, Brasil, 2015.
6. American Railway Engineering and Maintenance Association. *Manual for Railway Engineering*; AREMA: Lanham, MA, USA, 2020; Volume 1–2.
7. *Standards Australia—1085.14*; Railway track material—Part 14: Prestressed Concrete Sleepers. Australian Standard: Sydney, Australia, 2019.
8. Li, X.; Doh, S.I.; Jing, G.; Chong, B.W.; Suil, A.L.; Chin, S.C. A comparative review on American, European and Chinese standard for railway concrete sleeper. *Phys. Chem. Earth Parts A/B/C* **2021**, *124*, 103073. [CrossRef]
9. Remennikov, A.M.; Kaewunruen, S. Experimental load rating of aged railway concrete sleepers. *Eng. Struct.* **2014**, *76*, 147–162. [CrossRef]
10. Janeliukstis, R.; Kaewunruen, S. A Novel Separation Technique of Flexural Loading-Induced Acoustic Emission Sources in Railway Prestressed Concrete Sleepers. *IEEE Access* **2019**, *7*, 51426–51440. [CrossRef]
11. Farnam, S.M.; Rezaie, F. Part A—Experimental: Experimental Analysis of Crack Propagation in Pre-stressed Concrete Sleepers by Fracture Mechanics. *Int. J. Transp. Eng.* **2017**, *4*, 163–177.
12. Farnam, S.M.; Rezaie, F. Experimental Analysis of Fracture and Damage Mechanics of Pre-Stressed Concrete Sleepers B70: Part B Analysis. *Int. J. Transp. Eng.* **2017**, *5*, 17–29.
13. Jokūbaitis, A.; Valivonis, J.; Marčiukaitis, G. Analysis of strain state and cracking of cocnrete sleepers. *J. Civ. Eng. Manag.* **2016**, *22*, 564–572. [CrossRef]

14. Li, D.; Kaewunruen, S.; Robery, P.; Remennikov, A. Creep and Shrinkage Models for Railway Prestressed Concrete Sleepers: A review. In Proceedings of the 15th East-Asia Pacific Conference on Structural Engineering and Construction: Railway Infrastructure, Xi'an, China, 11–13 October 2017.
15. Li, D.; Kaewunruen, S.; Robery, P.; Remennikov, A.M. Creep and Shrinkage Effects on Railway Prestressed Concrete Sleepers. In *ICRT 2017: Railway Development, Operations, and Maintenance*; American Society of Civil Engineers: Reston, VA, USA, 2018; pp. 394–405.
16. Li, D.; Kaewunruen, S.; Robery, P.; Remennikov, A.M. Parametric Studies Into Creep and Shrinkage Characteristics in Railway Prestressed Concrete Sleepers. *Front. Built Environ.* **2020**, *6*, 130. [CrossRef]
17. Li, D.; You, R.; Kaewunruen, S. Mechanisms and evolution of cracks in prestressed concrete sleepers exposed to time-dependent actions. *Appl. Sci.* **2022**, *12*, 5511. [CrossRef]
18. Camille, C.; Hewage, D.K.; Mirza, O.; Clarke, T. Full-scale static and single impact testing of prestressed concrete sleepers reinforced with macro synthetic fibres. *Transp. Eng.* **2022**, *7*, 100104. [CrossRef]
19. de Azevedo, A.C.L.; Teixeira, A.M.A.J.; Carneiro, L.A.V. Flexural behavior of hybrid GFRP—Concrete railway sleepers. *IBRACON Struct. Mater. J.* **2019**, *12*, 738–765. [CrossRef]
20. Rezaie, F.; Farnam, S. Fracture mechanics analysis of pre-stressed concrete sleepers via investigating crack initiation length. *Eng. Fail. Anal.* **2015**, *58*, 267–280. [CrossRef]
21. Farnam, S.; Rezaie, F. Simulation of crack propagation in prestressed concrete sleepers by fracture mechanics. *Eng. Fail. Anal.* **2018**, *96*, 109–117. [CrossRef]
22. Soltanian, H.; Firouzi, A.; Mohammadzadeh, S. Time dependent reliability analysis of railway sleepers subjected to corrosion. *Struct. Concr.* **2018**, *19*, 1409–1418. [CrossRef]
23. Zi, G.; Moon, D.Y.; Lee, S.-J.; Jang, S.Y.; Yang, S.C.; Kim, S.-S. Investigation of a concrete railway sleeper failed by ice expansion. *Eng. Fail. Anal.* **2012**, *26*, 151–163. [CrossRef]
24. Comite Euro-Internacional Du Béton. *Model Code 2010—First Complete Draft*; Comite Euro-Internacional Du Béton: Lausanne, Switzerland, 2010.
25. *ASTM Standard A421*; Standard Specification for Stress-Relieved Steel Wire for Prestressed Concrete. ASTM International: West Conshohocken, PA, USA, 2021.
26. *ASTM Standard A881*; Standard Specification for Steel Wire, Indented, Low-Relaxation for Prestressed Concrete. ASTM International: West Conshohocken, PA, USA, 2017.
27. Associação Brasileira de Normas Técnicas. *NBR7482—Fios de Aço Para Estruturas de Concreto Protendido—Especificação*; Associação Brasileira de Normas Técnicas: Rio de Janeiro, Brasil, 2020.
28. Vilgis, T.; Boué, F. Deformation dependence of the form factor of a crosslinked chain in a rubber: Entanglement and orientational effect. *Polymer* **1986**, *27*, 1154–1162. [CrossRef]
29. Guerreiro, L. Isolamento Sísmico de Edifícios. Ph.D. Thesis, Departamento de Engenharia Civil, Instituto Superior Técnico, Lisbon, Portugal, 1997.
30. Associação Brasileira de Normas Técnicas. *NBR5739—Concreto—Ensaio de Compressão de Corpos e Prova Cilíndricos*; Associação Brasileira de Normas Técnicas: Rio de Janeiro, Brasil, 2018.
31. Associação Brasileira de Normas Técnicas. *NBR6349—Barras, Cordoalhas e Fios de Aço Para Armaduras de Protensão—Ensaio de Tração*; Associação Brasileira de Normas Técnicas: Rio de Janeiro, Brasil, 2022.
32. Cervenka, V.; Jandele, L.; Cervenka, J. *ATENA Program Documentation, Part 1: Theory*; Cervenka Consulting: Prague, Czech Republic, 2021.
33. Cervenka, V.; Cervenka, J.; Janda, Z.; Pryk, D. *ATENA Program Documentation, Part 8: User's Manual for ATENA-GiD Interface*; Cervenka Consulting: Prague, Czech Republic, 2021.
34. Cervenka, V.; Papanikolaou, V.K. Three dimensional combined fracture–plastic material model for concrete. *Int. J. Plast.* **2008**, *12*, 2192–2220. [CrossRef]
35. Menetrey, P.; William, J.K. Triaxial failure criterion for concrete and its generalization. *ACI Struct. J.* **1995**, *92*, 664.
36. Rashid, Y. Ultimate strength analysis of prestressed concrete pressure vessels. *Nucl. Eng. Des.* **1968**, *7*, 334–344. [CrossRef]
37. Bažant, Z.P.; Oh, B.H. Crack band theory for fracture of concrete. *Mater. Et Constr.* **1983**, *16*, 155–177. [CrossRef]
38. Rankine, W.J.M. *Manual of Applieds Mechanics*; Griffin: Glasgow, UK, 1876.
39. Hordijk, D.A. Local Approach to Fatigue of Concrete. Ph.D. Thesis, Delft University of Technology, Delft, The Netherlands, 1991.
40. Cervenka, V. Constitutive Model for Cracked Reinforced Concrete. *ACI Struct. J.* **1985**, *28*, 877–882.
41. Darwin, D.; Pecknold, D.A.W. *Inelastic Model for Cyclic Biaxial Loading of Reinforced Concrete*; Civil Engineering Studies; University of Illinois: Champaign, IL, USA, 1974.
42. Vecchio, F.J.; Collins, M.P. Modified Compression-Field Theory for Reinforced Concrete Beams Subjected to Shear. *ACI Struct. J.* **1986**, *83*, 219–231.
43. Crisfield, M.A.; Wills, J. The Analysis of Reinforced Concrete Panels Using Different Concrete Models. *J. Eng. Mech. ASCE* **1989**, *115*, 578–597. [CrossRef]
44. Souza, R.A. Concrete Estrutural: Análise e Dimensionamento de Elementos com Descontinuidade. Ph.D. Thesis, Poly-technic School, University of São Paulo, São Paulo, Brazil, 2004.

45. Pryk, D.; Cervenka, V. *ATENA Program Documentation, Part 11: Troubleshooting Manual*; Cervenka Consulting: Prague, Czech Republic, 2020.
46. Rots, J.G.; Blaauwendraad, J. Crack Models for Concrete: Discrete or Smeared? Fixed, Multi-Directional or Rotating? Heron: Delft, The Netherlands, 1989; Volume 34, pp. 1–60.
47. Torrenti, J.; Le Roy, R. Analysis of some basic creep tests on concrete and their implications for modeling. *Struct. Concr.* **2017**, *19*, 483–488. [CrossRef]
48. Acker, P.; Ulm, F.-J. Creep and shrinkage of concrete: Physical origins and practical measurements. *Nucl. Eng. Des.* **2001**, *203*, 143–158. [CrossRef]
49. Hillerborg, A. Results of three comparative test series for determining the fracture energy Gf of concrete. *Mater. Struct.* **1985**, *18*, 407–413. [CrossRef]
50. Wittmann, F.; Mihashi, H.; Nomura, N. Size effect on fracture energy of concrete. *Eng. Fract. Mech.* **1990**, *35*, 107–115. [CrossRef]
51. Sanabria, R.A.D.; Oliveira, L.H.B.; Trautwein, L.M.; Almeida, L.C.; Santos, A.C. Aspects of Finite Element Modeling of Punching Shear Behavior of Reinforced Concrete Flat Slabs. *Lat. Am. J. Solids Struct.* **2018**, *15*, e120. [CrossRef]

Disclaimer/Publisher's Note: The statements, opinions and data contained in all publications are solely those of the individual author(s) and contributor(s) and not of MDPI and/or the editor(s). MDPI and/or the editor(s) disclaim responsibility for any injury to people or property resulting from any ideas, methods, instructions or products referred to in the content.